



Production of gas-releasing electrolyte-replenishing Ah-scale zinc metal pouch cells with aqueous gel electrolyte

Received: 4 December 2022

Accepted: 3 July 2023

Published online: 14 July 2023

 Check for updates

Feifei Wang^{1,2,3,4}, Jipeng Zhang^{1,3}, Haotian Lu^{1,2,3,4}, Hanbing Zhu^{1,3}, Zihui Chen^{1,3}, Lu Wang^{1,2,3,4}, Jinyang Yu^{1,3}, Conghui You², Wenhao Li⁵, Jianwei Song⁵, Zhe Weng^{1,3}, Chunpeng Yang^{1,3}  & Quan-Hong Yang^{1,2,3} 

Aqueous zinc batteries are ideal candidates for grid-scale energy storage because of their safety and low-cost aspects. However, the production of large-format aqueous Zn batteries is hindered by electrolyte consumption, hydrogen gas evolution and accumulation, and Zn dendrites growth. To circumvent these issues, here we propose an “open” pouch cell design for large-format production of aqueous Zn batteries, which can release hydrogen gas and allow the refilling of the electrolyte components consumed during cell cycling. The cell uses a gel electrolyte containing crosslinked kappa (k)-carrageenan and chitosan. It bonds water molecules and hinders their side reaction with Zn, preventing electrolyte leakage and fast evaporation. As a proof-of-concept, we report the assembly and testing of a Zn | $Zn_xV_2O_5 \cdot nH_2O$ multi-layer “open” pouch cell using the carrageenan/chitosan gel electrolyte, which delivers an initial discharge capacity of 0.9 Ah and 84% capacity retention after 200 cycles at 200 mA g⁻¹, 370 kPa and 25 °C.

Due to their intrinsic safety and low-cost, aqueous zinc (Zn) batteries have great promise for use as grid-scale energy storage^{1–4}. However, the Zn anode suffers from problems including Zn dendrite growth and a parasitic hydrogen evolution reaction (HER) at the anode-electrolyte interface, especially in large-format cells (e.g., multi-layer pouch cells), and this compromises the safety of the batteries^{5–7}. Because metallic Zn is thermodynamically unstable in an acidic electrolyte, HER inevitably occurs on the Zn-electrolyte interface during Zn deposition, which decreases the Coulombic efficiency (CE) and cycling stability of the batteries^{8,9}. The excessive consumption of electrolyte may result in battery failure, and H₂ accumulation triggers battery swelling and even explosion¹⁰. There may also be dendrite growth due to the “tip effect” which produces dead Zn (i.e., Zn metal regions which are electronically disconnected from the current collector), aggravating hydrogen

evolution and even causing short circuits, all of which prevent the large-scale application of aqueous Zn batteries⁴.

Many efforts have been devoted to addressing these problems, such as using electrolyte additives, highly concentrated electrolytes¹¹, nonaqueous electrolytes¹², hydrogel electrolytes^{13–15}, 3D Zn anodes, and anode/electrolyte interface modification^{16–22} however, most studies were conducted in laboratory-based coin cells, which are quite different from the large-format Zn batteries required for large-scale energy storage^{3,23}. The coin-cell or even pouch-cell configurations of Zn batteries reported in the literature are generally adapted from Li-ion batteries^{24,25} which have a hermetically sealed closed system because they use hazardous and volatile organic electrolytes and air-sensitive electrode materials^{19,26}. However, using sealed Zn batteries not only neglects the fact that the Zn metal and aqueous electrolytes

¹Nanoyang Group, Tianjin Key Laboratory of Advanced Carbon and Electrochemical Energy Storage, School of Chemical Engineering and Technology, National Industry-Education Integration Platform of Energy Storage, and Collaborative Innovation Center of Chemical Science and Engineering, Tianjin University, Tianjin 300072, China. ²Joint School of National University of Singapore and Tianjin University, International Campus of Tianjin University, Fuzhou 350207, China. ³Haihe Laboratory of Sustainable Chemical Transformations, Tianjin 300192, China. ⁴Department of Chemistry, National University of Singapore, Singapore 117543, Singapore. ⁵State Key Laboratory for Strength and Vibration of Mechanical Structures, Xi'an Jiaotong University, Xi'an 710049, China. ✉ e-mail: cpyang@tju.edu.cn; qhyangcn@tju.edu.cn

are air-stable and environmentally-friendly but also imposes avoidable problems, such as H_2 accumulation and battery swelling (Fig. 1a and Supplementary Fig. 1)^{18,24,27–29}. We therefore propose an open system to resupply any consumed electrolyte component, taking advantage of the safe and abundant aqueous electrolyte, while avoiding the problems of gas accumulation and swelling, to improve the scale and life of the battery. However, other issues such as electrolyte leakage and evaporation could be the problem of the open-system configuration^{30–32}. Hydrogel electrolytes show potential in addressing these issues; however, most of the related studies are still limited to small cell size and capacity, not practical for application (Supplementary Table 1)^{33–35}.

Here, we report a refillable configuration for practical large-format aqueous Zn batteries, which is functioned with an open system for H_2 releasing and water refilling and a water-bonding gel electrolyte (Fig. 1b). The gel electrolyte is made of crosslinked biomass-derived kappa (κ)-carrageenan and chitosan, which alleviates electrolyte consumption, prevents battery swelling, and mitigates Zn dendrite growth. The crosslinked κ -carrageenan and chitosan (CarraChi) gel electrolyte has numerous polar functional groups ($-\text{OH}$, $-\text{NH}_2$, $-\text{SO}_4^{2-}$) that bond water molecules to suppress fast electrolyte evaporation and the HER. Moreover, the refillable, open-system battery configuration allows effective electrolyte replenishment and gas release in a multi-layer pouch cell configuration. As a result, using the CarraChi gel in refillable, large-format Zn batteries improves the plating/stripping reversibility, cycling stability, and cell lifespan. The refillable symmetric pouch cells demonstrate a life of ~4000 h at a current density of 10 mA cm^{-2} with an areal capacity of 35 mAh cm^{-2} , achieving a cumulative capacity of 1286 Ah. In addition, a $\text{Zn} \parallel \text{Zn}_x\text{V}_2\text{O}_5 \cdot n\text{H}_2\text{O}$ multi-layer pouch cell using the refillable configuration has a high capacity (0.9 Ah) and good cycling stability, retaining 84% capacity after 200 cycles.

Results

Water-bonding gel electrolyte

As a critical component of the refillable Zn battery, the water-bonding CarraChi gel was prepared by crosslinking κ -carrageenan and chitosan using a simple mixing-casting method and subsequent immersion in 2 M ZnSO_4 (Fig. 2a). The protonated $-\text{NH}_3^+$ in chitosan interacts with $-\text{SO}_4^{2-}$ in κ -carrageenan through electrostatic interactions while the $-\text{OH}$ functional groups in CarraChi gel can form hydrogen bonds with H_2O to decrease the water activity, which is expected to suppress the HER³⁶. The κ -carrageenan and chitosan

were respectively obtained from biomass-based carrageenan and crustaceans. These raw materials ensure the production of the CarraChi solution (Supplementary Fig. 2) and the manufacture of the CarraChi gel by a cast-dry process (Fig. 2b, c). Our rolling and bending tests also prove the feasibility of using the CarraChi membrane in lamination and winding technology for practical battery manufacture (Supplementary Fig. 3a). Scanning electron microscopy (SEM) shows that the morphology of the as-prepared CarraChi membrane is smooth and dense (Supplementary Fig. 3b) with a thickness of $18 \mu\text{m}$ (Fig. 2d).

We investigated the crosslinking of κ -carrageenan and chitosan by X-ray photoelectron spectroscopy analysis (XPS) (Supplementary Fig. 4a, Supplementary Table 2). The N1s XPS spectrum of dry CarraChi gel contains two peaks at 400.3 and 399.5 eV which are respectively ascribed to N-H and C-N bonds in the chitosan (Supplementary Fig. 4b)³⁷. In the S2p spectrum, the peaks at 168.9 and 170.1 eV respectively correspond to the $\text{S}2p_{3/2}$ and $\text{S}2p_{1/2}$ of the sulfate groups in the κ -carrageenan (Supplementary Fig. 4c)³⁸. We also studied the chemical bonding of the CarraChi gel, in comparison with κ -carrageenan and chitosan, by Fourier-transform infrared (FTIR) spectra (Fig. 2e). In the FTIR spectrum of CarraChi gel, the peaks at 1558 and 1449 cm^{-1} are respectively ascribed to the N-H and C-N stretching vibrations in chitosan³⁷, and the peak at 1219.4 cm^{-1} is attributed to the sulfate stretching of $\text{S}=\text{O}$ in κ -carrageenan³⁹. In addition, a red shift of the $-\text{OH}/-\text{NH}_2$ peak in CarraChi gel is observed, indicating the crosslinking interaction between chitosan and κ -carrageenan.

Due to the abundant hydrogen bonds and electrostatic interactions between the κ -carrageenan and chitosan, the CarraChi- ZnSO_4 has much higher strain-to-failure (45%) and tensile strength (14.2 MPa) than the commercial glass fiber (GF) separator (6% and 0.3 MPa) and a κ -carrageenan- ZnSO_4 membrane (32% and 4.2 MPa) (Fig. 2f and Supplementary Fig. 5). Compared to the wet CarraChi gel (CarraChi- H_2O), the mechanical strength increased after the Zn^{2+} addition, possibly due to the bonding effect between divalent Zn^{2+} and $-\text{SO}_4^{2-}/-\text{OH}$ functional groups in the hydrogel network^{40,41}. Such an improved mechanical property of the CarraChi gel electrolyte is expected to facilitate electrode fabrication and battery assembling⁴².

Zn deposition with the gel electrolyte

The CarraChi gel electrolyte shows good electrochemical properties for aqueous Zn batteries. It has a high ionic conductivity of 5.3 mS cm^{-1}

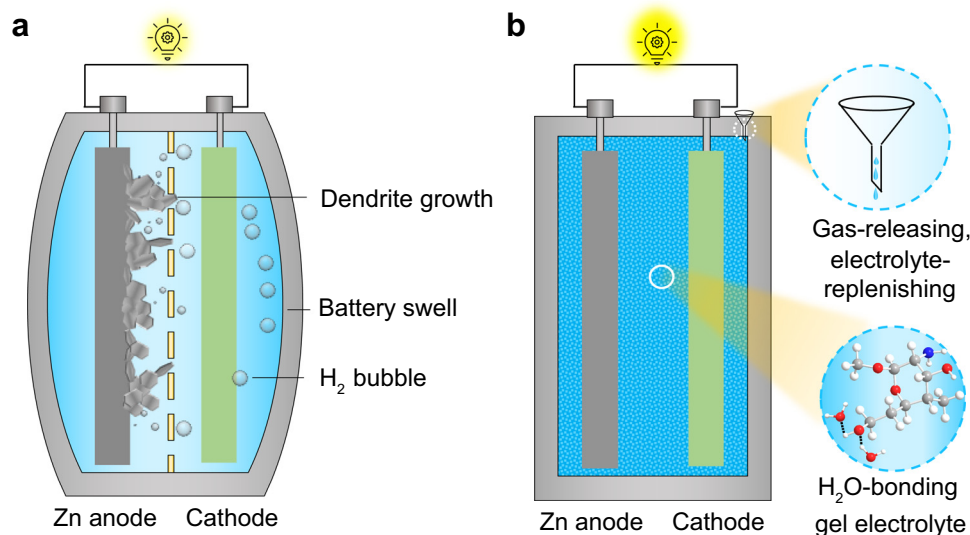


Fig. 1 | Schematics of Zn batteries operating in two configurations. **a** A closed system and **b** an open system. Compared to the closed-system battery with problems such as Zn dendrite formation and H_2 evolution, the open-system battery with H_2O injection and the gas outlet could improve the cycling life of the cell.

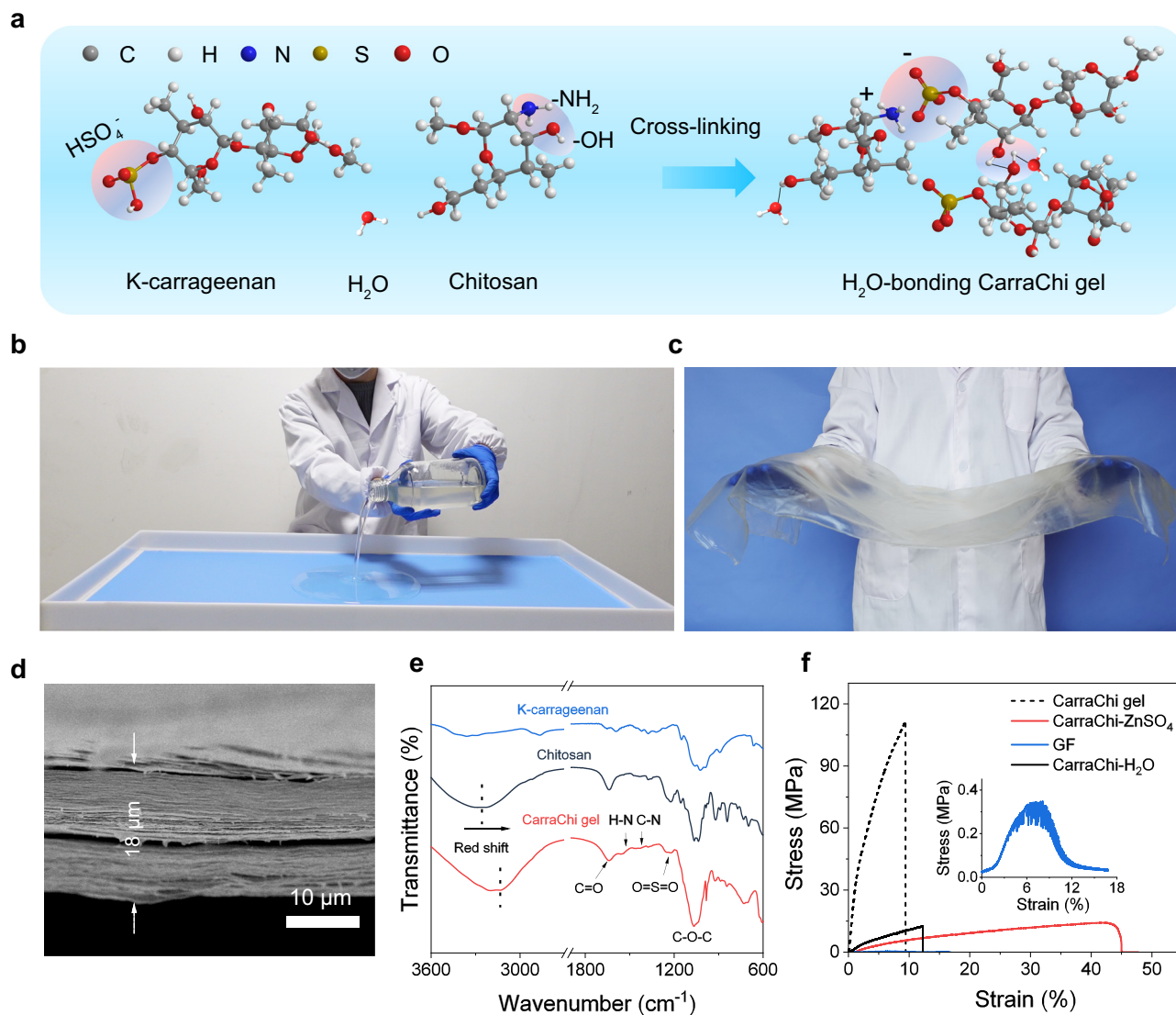


Fig. 2 | Fabrication and physical properties of the CarraChi gel. **a** Crosslinked structure of the CarraChi gel. **b** Photo of the cast-drying fabrication process of the CarraChi gel. **c** Photo of a CarraChi gel membrane. **d** Side-view SEM image of the dry

CarraChi gel. **e** FTIR spectra of the dry CarraChi gel, chitosan, and k-carrageenan at 25 °C. **f** Stress–strain curves of the dry CarraChi gel, CarraChi-H₂O, CarraChi soaked with ZnSO₄, and GF at 25 °C.

at 25 °C, which allows Zn²⁺ ion migration through CarraChi at a high current rate. We used linear scanning voltammetry (LSV) to investigate the electrochemical stability window of the CarraChi gel electrolyte (Supplementary Fig. 6) and found that it has a high oxidation potential of more than 2.26 V (vs. Zn²⁺/Zn) compared to that of a ZnSO₄ solution (1.99 V vs. Zn²⁺/Zn). The Zn²⁺ transference numbers (t_{Zn}) of CarraChi, and GF separator with ZnSO₄ electrolyte have also been obtained using the Bruce-Vincent method⁴³, and the CarraChi gel electrolyte has a high t_{Zn} of 0.52, which exceeds that of the aqueous electrolyte with commercial GF (0.29), indicating the improved Zn²⁺ transfer property in CarraChi gel electrolyte (Supplementary Fig. 7, Supplementary Table 3).

Due to the numerous oxygen-containing functional groups in k-carrageenan and chitosan, the CarraChi gel has a negatively charged surface, as shown by its negative zeta potentials (−54 mV) (Fig. 3a). After the addition of ZnSO₄, the less negative zeta potential of −9.4 mV reveals the effective adsorption or crosslinking of Zn²⁺ by the CarraChi gel, facilitating the desolvation of Zn²⁺ during the deposition process, which differs from GF separator without adsorption toward Zn²⁺ (Supplementary Fig. 8). The desolvation process of Zn²⁺ ion is usually considered to be the rate-determining step for Zn deposition, and its

activation energy (E_a) can be obtained using the Arrhenius equation:

$$\frac{1}{R_{\text{ct}}} = Ae^{-\frac{E_a}{RT}} \quad (1)$$

where R_{ct} is the charge transfer resistance at the electrode/electrolyte interface, A is the frequency factor, R is the gas constant, and T is the absolute temperature^{44,45}. The Zn|CarraChi|Zn cell shows a much smaller R_{ct} than that of the Zn|GF|Zn cell with ZnSO₄ electrolyte at temperatures ranging from 25 to 50 °C (Supplementary Fig. 9, Supplementary Tables 4 and 5), confirming the improved charge transfer ability of the CarraChi gel electrolyte. The calculated E_a of the Zn|CarraChi|Zn cell is 27.9 kJ mol^{−1}, which is only 54.5% of that of the Zn|GF|Zn cell (51.2 kJ mol^{−1}) (Fig. 3b), proving easier desolvation in the CarraChi gel electrolyte.

We used Raman spectroscopy to explore the solvation configuration in the CarraChi gel electrolyte (Supplementary Fig. 10). In comparison to the ZnSO₄ aqueous solution, the proportion of strong H-bonding water reduces while weak H-bonding water increases in the CarraChi-ZnSO₄, suggesting the bonding between the CarraChi gel and H₂O molecules and reconstruction of the H-bond network of free H₂O, which are expected to limit HER^{29,46,47}. The suppressed HER on the Zn

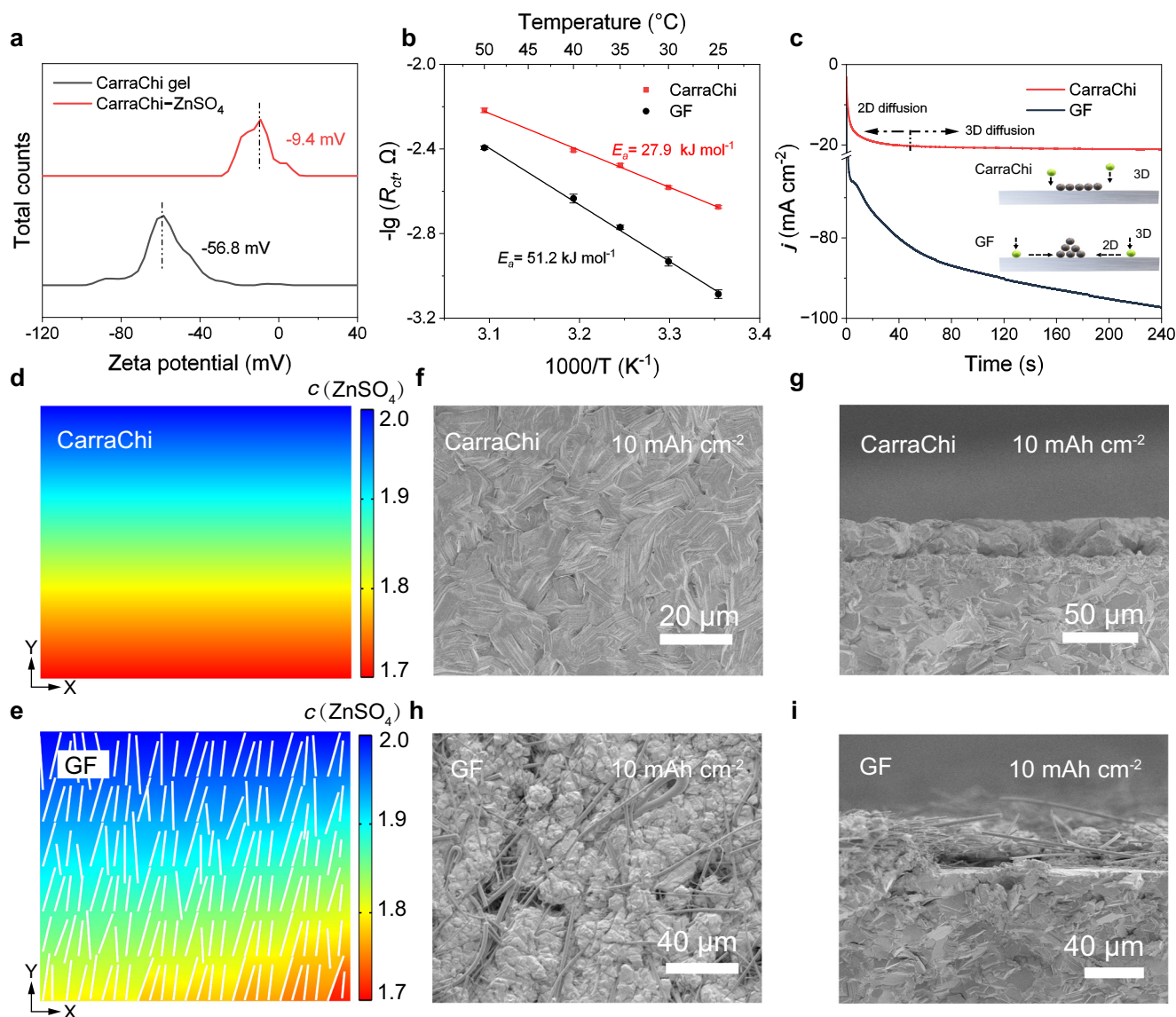


Fig. 3 | The mechanism of the CarraChi gel electrolyte guiding uniform Zn deposition. **a**, Zeta potential of the CarraChi gel electrolyte in an aqueous solution before and after the addition of ZnSO_4 (25 °C). **b**, Calculated desolvation energy of Zn^{2+} with a CarraChi gel electrolyte and a GF separator (The error bar represents the error of the fitted R_{ct} value, Supplementary Tables 4 and 5). **c**, Chronoamperometry curves of symmetric devices at a constant potential of -150 mV at 25 °C (inset: schematics of the Zn^{2+} diffusion and reduction on the Zn anode and Zn-CarraChi

surfaces). Simulated Zn^{2+} concentration distribution inside **d**, Zn|CarraChi|Zn symmetric cells and **e** Zn|GF|Zn symmetric cells at 10 mA cm^{-2} (the thin strip represents glass fiber) (c represents concentration, M). **f–i** SEM images of deposited Zn in coin cells at 25 °C (10 mA cm^{-2} with deposition capacity of 10 mAh cm^{-2}): **f** top and **g**, side views with the CarraChi gel electrolyte; **h** top and **i**, side views with the GF separator.

anode with CarraChi is also proved by a lower onset overpotential (-1.37 V vs. standard hydrogen electrode, SHE) than that with a GF separator (-1.28 V vs. SHE) (Supplementary Fig. 11). In situ optical microscope images further reveal the good suppression of the HER in the competing reactions between Zn deposition and HER on the Zn anode (Supplementary Fig. 12). The CarraChi gel electrolyte also reduces corrosion reactions between the Zn foil and ZnSO_4 , which is proved by the weaker peak intensity of by-products in the X-ray diffraction (XRD) patterns and the smooth surface in the SEM images in the anti-corrosion experiment (Supplementary Fig. 13).

We also conducted chronoamperometry tests to understand the mechanisms of Zn deposition behaviors at the Zn-CarraChi interfacial sites (Fig. 3c). In the symmetric cell with GF, the response current increased continually beyond 240 s, indicating non-uniform Zn deposition due to the random planar diffusion of Zn ions. In contrast, the response current of Zn-CarraChi stopped increasing within 40 s,

indicating that the surface 2D diffusion process on the Zn surface is suppressed with the CarraChi gel electrolyte⁴⁸. Generally, the absorbed Zn ions tend to diffuse along the surface to energetically favorable sites (tip sites or defective areas) to minimize their energy on the Zn surface. Due to the abundant $-\text{OH}$ and $-\text{SO}_4^{2-}$ functional groups, the CarraChi gel adhered on Zn foil would provide an extra interfacial energy barrier to prevent 2D Zn^{2+} diffusion. Meantime, the abundant Zn^{2+} transport channels in the crosslinked gel framework render the Zn^{2+} flux uniform. Therefore, a stable and uniform deposition of Zn is formed on the Zn metal anode (Fig. 3c, inset). Using finite-element simulation, we further reveal that the uniform Zn deposition is attributed to the homogenized Zn^{2+} concentration and electric field near the Zn-CarraChi interface (Fig. 3d, e and Supplementary Fig. 14).

Ex situ SEM images show that uniform Zn deposition was obtained with the CarraChi gel electrolyte as the deposition capacity increased from 10 to 30 mAh cm^{-2} , which is ascribed to the fast desolvation

kinetics that homogenizes the Zn^{2+} flux and electric field at the electrolyte-electrode interface (Fig. 3f, g, and Supplementary Fig. 15a, b). In contrast, Zn is deposited in the pores of the GF separator with a capacity of 10 mAh cm^{-2} (Fig. 3h, i), followed by the short circuit of the symmetric cell when the capacity increases to 20 mAh cm^{-2} , ascribable to the penetration of the Zn metal depositions in the GF separator (Supplementary Fig. 15c, d).

Long-life Zn battery performance

To test the rate performance and long-term stability of the Zn anode, we performed galvanostatic cycling of symmetric cells using the CarraChi gel electrolyte and the GF separator. The Zn|CarraChi|Zn cell has a good rate performance and stable cycling even at a high current density of 40 mA cm^{-2} compared to the short circuit of the Zn|GF|Zn cell (Fig. 4a). The Zn|CarraChi|Zn cell also shows good cycling stability and long cycling life of over 2500 h at 1 mA cm^{-2} with a capacity of 1 mAh cm^{-2} , which is nearly 50 times that of the Zn|GF|Zn cell (Supplementary Fig. 16). Even at a higher current density of 10 mA cm^{-2} with a high areal capacity of 120 mAh cm^{-2} , corresponding to a 65% depth of discharge (DOD), a symmetric cell with CarraChi gel electrolyte also shows improved cycling stability with a lifespan of over 180 h (Fig. 4b). Such a high capacity, current density, and DOD are hardly possible for closed-system Zn batteries with GF separators⁴⁹. We used SEM to characterize the changes of the Zn surfaces after 5 cycles at 10 mA cm^{-2} with a capacity of 10 mAh cm^{-2} . Compared with the short circuit of the symmetric cell with GF, the Zn anode with the CarraChi gel electrolyte has a smooth Zn surface, indicating uniform Zn plating/stripping during cycling (Fig. 4c). Moreover, in comparison to the unstable Zn plating/stripping less than 100 cycles with GF separator, the Zn anode with CarraChi gel electrolyte displays a stable CE for 600 cycles at 5 mA cm^{-2} , which is as high as 99.8% after 300 cycles (Fig. 4d, e).

With these advantages of the CarraChi gel electrolyte, we developed a Zn pouch cell with a refillable configuration (Fig. 4f). The size of the Zn electrode was $8 \text{ cm} \times 8 \text{ cm}$, which can be further increased due to the scalability of the CarraChi gel. The pouch symmetric cell has an opening for water refilling and H_2 release, which provides a way to supplement the electrolyte and for pressure release. The pouch cell has a long life of $\sim 4000 \text{ h}$ (65% DOD) with an areal capacity of 35 mAh cm^{-2} at 10 mA cm^{-2} (Fig. 4g). When the overpotential increased markedly due to electrolyte consumption during cycling, pure water or 2 M ZnSO_4 was refilled to sustain the ionic conductivity for normal operation, which is indicated in the voltage-time curves (Fig. 4g). The electrochemical impedance spectroscopy (EIS) curves before and after cycling also confirm that no short circuit occurred during cycling (Fig. 4h). The cells with the refillable configuration also demonstrate an areal capacity per cycle (35 mAh cm^{-2}), and a good cumulative capacity (1286 Ah) and average CE ($\sim 99.5\%$), which exceed the Zn||Zn state-of-the-art performance (Fig. 4i and Supplementary Table 6)^{38,39,50–57}. In contrast, the Zn|GF|Zn pouch cell exhibits limited capacity, and a short circuit occurs when the current density increases to 2 mAh cm^{-2} (Supplementary Fig. 17).

To explore the practical use of the CarraChi gel electrolyte, we coupled Zn metal anodes with $\text{Zn}_x\text{V}_2\text{O}_5 \cdot n\text{H}_2\text{O}$ (ZVO) cathodes in coin cell configuration. The ZVO was prepared using a previously published method, and it gave the same SEM images and XRD patterns as reported (Supplementary Fig. 18)^{58,59}. The Zn|CarraChi|ZVO cell had high specific capacities of 349.6 mAh g^{-1} at 0.2 A g^{-1} and 200 mAh g^{-1} at 4 A g^{-1} (based on active ZVO mass) in comparison to that of Zn|GF|ZVO cells (Fig. 5a, Supplementary Fig. 19), implying the fast redox kinetics of the Zn|CarraChi|ZVO. As the specific current increased to 8 A g^{-1} , a high specific capacity of 115.6 mAh g^{-1} was retained, which is much better than that of Zn|GF|ZVO cells (71.1 mAh g^{-1} , 20% capacity retention) (Fig. 5b). In addition, the Zn|CarraChi|ZVO cell had a high specific capacity of 275.8 mAh g^{-1} when the specific current recovered to 1 A g^{-1} , indicating its good rate performance.

The improved cycling stability due to effective suppression of dendrite and ZVO dissolution ensures the long life of the Zn batteries (Supplementary Fig. 20). Figure 5c shows the cycling stability of Zn|CarraChi|ZVO and Zn|GF|ZVO cells for 100 cycles at 0.2 A g^{-1} . Compared to the fast short circuit and lower CE of the Zn|GF|ZVO cell, the Zn|CarraChi|ZVO cell showed good capacity retention of 88.2% with an average CE of nearly 100%.

We carried out EIS measurements and analyses, and observed the morphology of the Zn||ZVO coin cells before and after cycling. Both Zn||ZVO coin cells had a low ohmic resistance (R_s) due to the high ionic conductivity of the aqueous electrolyte (Supplementary Fig. 21a, Supplementary Table 7). Meanwhile, a lower initial charge-transfer resistance was obtained for the Zn|CarraChi|ZVO cell compared to that for the Zn|GF|ZVO cell. Even after cycling, a smaller R_{ct} was measured for the Zn|CarraChi|ZVO cell in comparison to the Zn|GF|ZVO cell (Supplementary Fig. 21b). These results clearly show the faster charge transfer and plating/stripping kinetics of Zn with the CarraChi gel electrolyte.

Optical images show that the CarraChi gel retains its initial integrity and transparency (Supplementary Fig. 22a), associated with its high mechanical strength and extensibility. In contrast, the GF became mixed with the cycled Zn due to the “pore-filling effect”⁶⁰. SEM images also show that the cycled Zn electrode with CarraChi had a smooth surface with uniform Zn deposition compared with the rough surface of cycled Zn electrode with GF which contained numerous dendrites (Supplementary Fig. 22b, c).

Considering the high mechanical strength and extensibility of the CarraChi membrane, we also assembled an $8 \text{ cm} \times 8 \text{ cm}$ pouch cell by lamination technology and tested its cycling stability (Fig. 5d, e). The Zn||ZVO multi-layer pouch cell with the CarraChi gel electrolyte and open configuration has an initial capacity of 0.9 Ah and good cycling stability, retaining 84% capacity after 200 cycles at 200 mA g^{-1} (based on active ZVO mass), which is better than the Zn||ZVO pouch cells with liquid electrolytes and GF separator (Fig. 5f and Supplementary Fig. 23). This performance is also better than that of the previously reported aqueous Zn metal pouch cells with V-based cathodes (Supplementary Table 8)^{61–67}. We ascribe the improved cycling stability to the open, refillable battery configuration, as well as the high strength of the CarraChi, inhibition of side reactions, and dendrite-free Zn plating/stripping caused by the uniform ion flux at the Zn-CarraChi interfaces. The open system allows gas release and electrolyte supplement, and prevents electrolyte depletion and battery swelling.

Discussion

We have reported an open, refillable battery configuration toward practical large-format aqueous Zn metal batteries, using a water-bonding gel electrolyte composed of k-carrageenan and chitosan, which prevents electrolyte consumption and battery swelling, and achieves Ah-scale capacity Zn batteries for large-scale energy storage. The crosslinked CarraChi gel contains abundant polar functional groups ($-\text{OH}$, $-\text{NH}_2$, $-\text{SO}_4^{2-}$) to bond H_2O molecules, thus suppressing the fast water evaporation and the HER. As a result, the open and refillable Zn symmetric cells deliver improved plating/stripping capacity, cycling stability, and long life. The open, refillable pouch cells realize a life of $>4000 \text{ h}$ at a current density of 10 mA cm^{-2} with an areal capacity of 35 mAh cm^{-2} and a DOD of 65%, giving a cumulative capacity of 1286 Ah. A Zn||ZVO multi-layer pouch cell with the CarraChi gel electrolyte and refillable configuration has a high capacity (0.9 Ah) and good cycling stability, retaining 84% capacity after 200 cycles.

Methods

Chemicals

Chitosan (D.D $\geq 95\%$, Aladdin), k-carrageenan (99%, Aladdin), ZnSO_4 (ACS purity grade, 99%, Aladdin), V_2O_5 (99.95% trace metals basis, Alfa

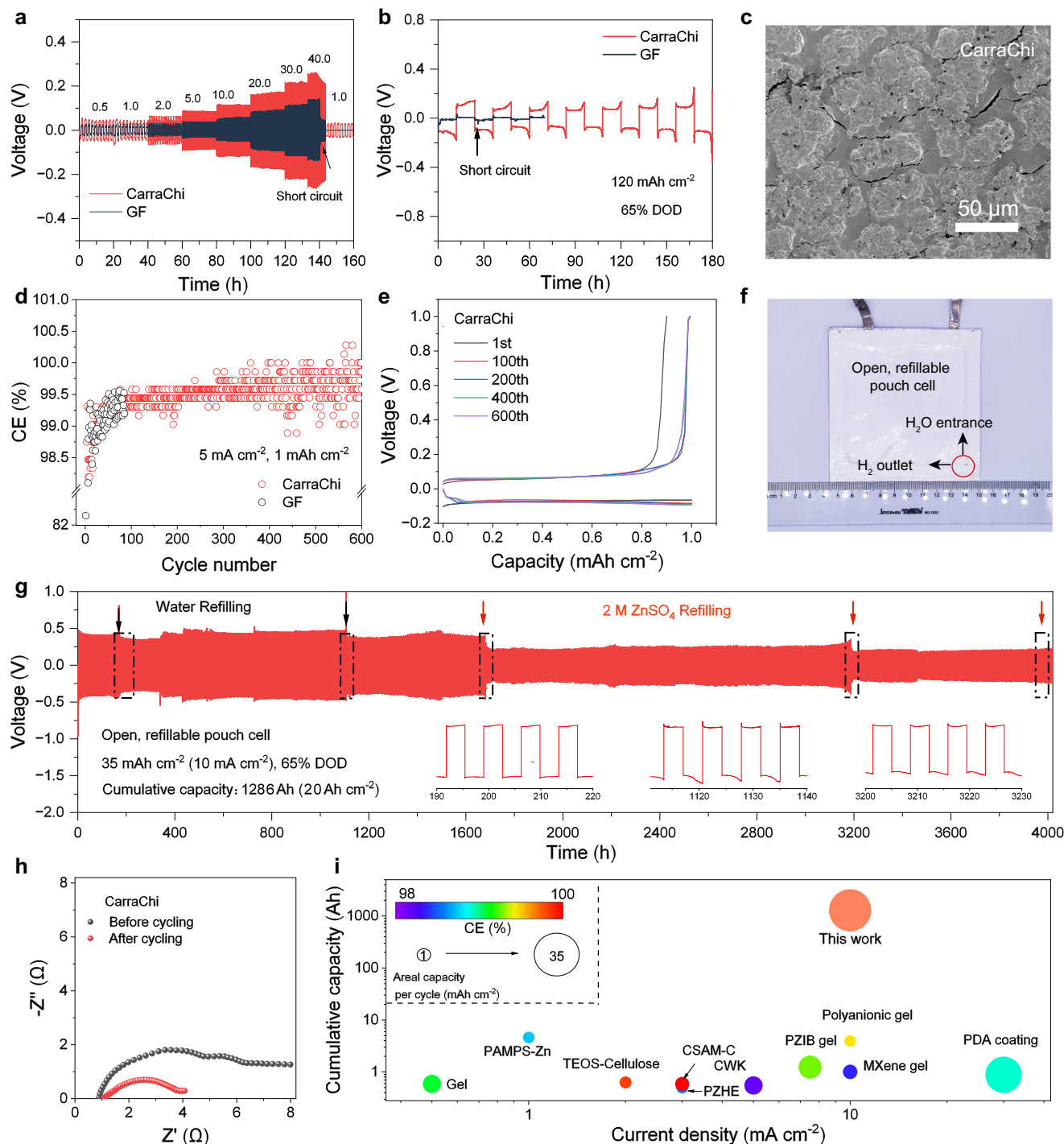


Fig. 4 | Testing of Zn metal electrode in symmetric coin and refillable pouch cell configurations at 25 °C. **a** Rate performance of Zn symmetric cells during Zn stripping/plating at current densities from 0.5 to 40 mA cm⁻² with CarraChi gel electrolyte or the GF separator. **b** Cyclic performance of Zn symmetric cells in coin cells at 10 mA cm⁻² with a plating/stripping capacity of 120 mAh cm⁻². **c** SEM image after 10 cycles at 10 mA cm⁻² (10 mAh cm⁻²) using the CarraChi gel electrolyte. **d** CE values of Zn plating/stripping in Zn|CarraChi|Cu and Zn|GF|Cu cells at 5 mA cm⁻² with a capacity of 1 mAh cm⁻². **e** Galvanostatic voltage profiles of the Zn|CarraChi

Cu cell. **f**, Optical image of the Zn|CarraChi|Zn pouch cell with the open and refillable configuration (8 cm × 8 cm). **g** Cycling performance of pouch Zn symmetric cells at 10 mA cm⁻² with the refillable system (inset: enlarged voltage-time curves). **h** EIS curves of the Zn|CarraChi|Zn symmetric cells before and after cycling (charging state) for 4000 h. **i** Performance comparison of the Zn|CarraChi|Zn pouch cell with other Zn symmetric cells reported in the literature, showing the CE, current density, and cumulative capacity (color represents the CE values).

Aesar), Zinc acetate (Zn(Ac)₂, ACS purity grade, 98%, Aladdin), N-methyl-2-pyrrolidone (NMP, 99%, Aladdin), deionized water (18.2 MΩ cm⁻¹), Super P carbon (99.5%, Guangdong Canrd New Energy Technology Co., Ltd, particle size of 40 nm).

Preparation of the CarraChi gel electrolyte

1g chitosan was added to 1000 ml deionized water under magnetic stirring for 1 week at 25 °C. The saturated chitosan solution was obtained by filtrating this solution to remove any undissolved material.

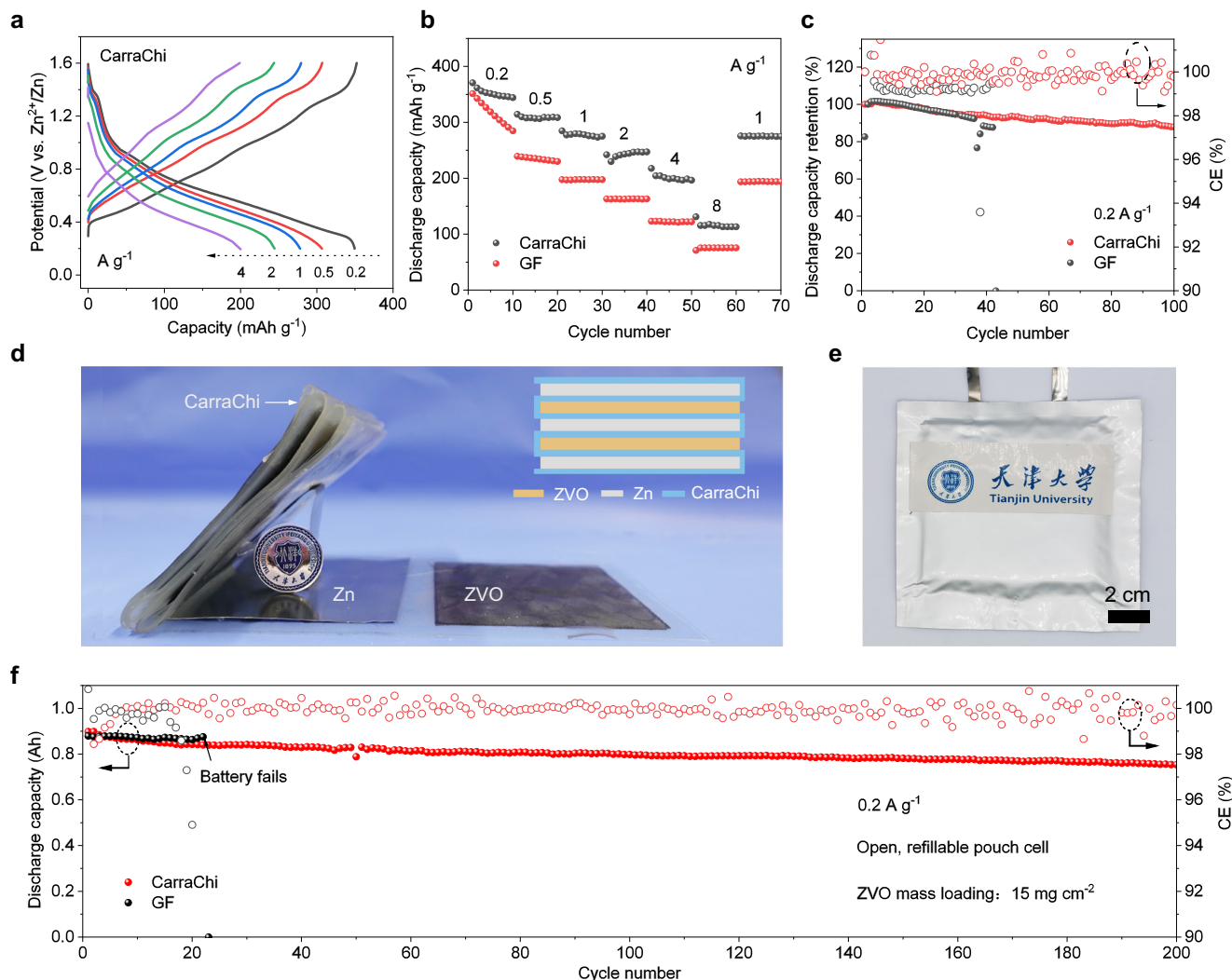


Fig. 5 | Application of CarraChi gel electrolyte in Zn||ZVO coin and pouch cell configuration (25 °C). These measurements are based on the active ZVO mass in coin cells **a–c**: **a** Voltage profiles of Zn||CarraChi||ZVO at various charge/discharge specific currents. **b** Comparison of the rate performance of Zn||CarraChi||ZVO and Zn||GF||ZVO batteries at different specific currents from 0.2 to 10 A g⁻¹. **c** Capacity

retention and CE curves of the Zn||CarraChi||ZVO battery in a cycling test at 0.2 A g⁻¹ compared to those of a Zn||GF||ZVO battery. **d** Schematic of the lamination process and corresponding side view optical image of the laminated Zn||CarraChi||ZVO. **e** The Zn||CarraChi||ZVO pouch cell. **f** Cycling stability of the pouch cell with CarraChi and GF at 0.2 A g⁻¹ (based on active ZVO mass, 25 °C).

The concentration of the saturated chitosan solution is $\sim 0.18 \text{ g L}^{-1}$ at 25 °C. To prepare the CarraChi gel precursor solution, 1 g k-carrageenan was dispersed in 100 ml of the saturated chitosan solution with magnetic stirring for 3 days. 50 ml of the as-prepared solution was cast into a PTFE mold with a diameter of 9 cm and allowed to stand for drying in the air environment. The obtained pure CarraChi was immersed in a 2 M ZnSO₄ solution (12 hours) for use (CarraChi).

Preparation of the Zn_xV₂O₅·nH₂O cathode

A total of 3 mmol of commercial V₂O₅ and 2.4 mmol of Zn(Ac)₂ were dissolved in 70 mL deionized water, then 5 mL acetone and 2 mL 10 wt % HNO₃ were then added to the solution with wet ultrasonication (70 W) in water for 5 min. The mixture was transferred to a 100 mL Teflon-lined autoclave (Anhui Kemi Machinery Technology Co., Ltd) and heated at 180 °C for 24 h. After natural cooling, the Zn_xV₂O₅·nH₂O powder was obtained after filtration and washing with deionized water, followed by drying in a vacuum at 80 °C for 12 h.

Material characterization

Scanning electron microscopy (SEM, Hitachi S4800) was used to characterize the morphology and elements. The cycled cells were

disassembled under an air environment and the electrodes were taken out and rinsed with ethanol several times to wash away any electrolyte salt and attached glass fiber. The electrodes were air-dried at 25 °C and then carefully transferred into the SEM sample chamber. A cross-sectional SEM photo was taken to measure the deposition thickness of Zn after a similar process. XRD patterns were collected on a Bruker D-8 diffractometer (Cu K α radiation, $\lambda = 0.154 \text{ nm}$) at 25 °C. The XPS measurements were conducted using an ESCALAB 250Xi (Thermo Fisher) with a monochromatic Al K α source. Raman spectra were tested by a LabRAM HR spectrometer from Horiba, which was equipped with an argon ion laser operating at a wavelength of 532 nm. The FTIR technique, performed using the Thermo Scientific Nicolet iS20 instrument, was utilized to acquire the relevant data concerning the covalent bonds. A mechanical testing machine (SUST CMT-1103) operating at a strain rate of 1.0 mm min⁻¹ was employed to evaluate the mechanical properties of the separators and gel electrolyte. Zeta potential measurements were conducted using the ZETA SIZER Nano series at 25 °C. The GF separator was ground and pulverized into powders for testing zeta potential. The anti-corrosion test included assembling symmetric cells with GF/ZnSO₄ and CarraChi gel electrolytes, respectively, and allowing them to remain undisturbed under open-circuit voltage for

one week. Afterward, the Zn electrodes were extracted, rinsed with deionized water, and air-dried at 25 °C for further characterization.

Assembly of coin cells

Zn foils (99.999%, Chengshuo) were polished with 1000 mesh sandpaper and directly used as Zn electrodes. 2032-type coin cells were assembled with two identical Zn foils ($d = 10$ mm, the thickness of 100 μm) after polishing. CarraChi gel or a GF (type A, Whatman, thickness of 0.26 mm, porosity of 90%, average pore of 0.7 μm) was used as the separator. For full cells, the cathodes were made by casting a mixture that contained ZVO powder (70 wt%), Super P carbon (20 wt%), and PVDF (10 wt%), onto a carbon cloth (produced by CeTech, porosity: 77%, thickness: 10 μm , denoted as CC). The CC loaded with ZVO (ZVO/CC), Zn foil, and CarraChi were used as the cathode, anode, and electrolyte, respectively (the mass loading of the active ZVO in the cathode: 1 mg cm^{-2}).

Assembly of pouch cell

The pouch symmetric cell was assembled with two identical Zn foils (8×8 cm^2) polished with 1000 mesh sandpaper. CarraChi gel, or a GF (GF-A, Whatman) was used as the separator. As for the pouch full cell, the ZVO was coated on carbon cloth (8×8 cm^2) with Super P and PVDF binders (the ZVO mass loading of 15 mg cm^{-2}), and the CarraChi gel electrolyte was cut into custom size for lamination and winding. Concerning the Zn|CarraChi|ZVO pouch cell, a pre-operation injection of 2 ml of 2 M ZnSO_4 solution was carried out. As for the Zn|GF|ZVO pouch cell, the previously mentioned gel electrolyte has been replaced with a GF separator, and concurrently, a 5 ml injection of 2 M ZnSO_4 is administered. Ti foil (1×4 cm^2) was connected with the current collector as the tab. After lamination, the assembled battery was encapsulated in an aluminum-plastic film. A pore was punched on the side of the sealing bag away from the tag. The water refilling procedure was conducted when the overpotential increased in comparison to the initial overpotential, and 0.5 ml g^{-1} (ratio of electrolyte to the active ZVO) electrolyte was injected every time. The pouch cell is subjected to a pressure of 370 kPa and a temperature of 25 °C during the electrochemical measurements.

Electrochemical measurements

Galvanostatic charge and discharge measurements were carried out with a Neware battery test system. The specific currents and discharge capacities in full cells are calculated based on the mass of active ZVO in the cathode. To improve the reproducibility of the experiment, we conducted a minimum of two repetitions for the electrochemical performance. The cycling stability tests were performed at various specific currents. LSV was performed on an Autolab Analyzer PGSTAT 128 N (Metrohm, Switzerland). EIS was measured on an IVIUM electrochemical station. For the HER test, the LSV was tested in a 1.0 M Na_2SO_4 aqueous solution, with a scan rate of 5 mV s^{-1} . The EIS tests were measured in the potentiostatic method, the frequency is in the range from 0.1 Hz to 100 kHz at open circuit potential and an amplitude of 5 mV. The open-circuit voltage time applied before EIS is 10 min, and the data number of EIS is 61. The ionic conductivity of the CarraChi gel was tested by two blocking electrodes (stainless steel, denoted as SS; Tianjin Yide times Technology Development Co., LTD; thickness: 100 μm ; diameter: 1 cm) and calculated according to the following equation:

$$\sigma = \frac{l}{RS} \quad (2)$$

where R is the resistance according to EIS measurement (2.5 Ω), L is the thickness of the CarraChi gel (0.105 mm), and S is the area of the contact between the SS and the gel (0.785 cm^2). The ionic conductivity of the CarraChi gel electrolyte was determined to be $\sigma = 5.3 \text{ s mS cm}^{-1}$.

Finite-element simulation of symmetric cells

A two-dimensional continuum model was used to investigate the ionic and potential distributions in Zn metal symmetric cells (Zn|CarraChi|Zn, Zn|GFA|Zn) at a constant current density ($i_0 = 10$ mA cm^{-2})^{68,69}. In CarraChi and ZnSO_4/GF electrolytes, there are the mass balance and the charge conservation. The ionic flux density was described by the Nernst-Planck equation with diffusion and migration terms. At the Zn-electrolyte interface, the boundary conditions were set according to the cell test system. The other boundaries were set as no flux. All finite-element simulations were conducted in COMSOL Multiphysics 6.1. The initial conditions and ionic diffusion coefficients were set to be consistent with the electrochemical measurement conditions and results.

Reporting summary

Further information on research design is available in the Nature Portfolio Reporting Summary linked to this article.

Data availability

The data that support the findings of this study are available in the online version of this paper and the accompanying Supplementary Information, or available from the corresponding authors on reasonable request. The source data underlying Figs. 2e, f, 3a–c, 4a, b, d, e, g, h, and 5a–c, f are provided as a Source Data file. Source data are provided with this paper.

References

- Wang, F. et al. Highly reversible zinc metal anode for aqueous batteries. *Nat. Mater.* **17**, 543–549 (2018).
- Sun, W. et al. A rechargeable zinc-air battery based on zinc peroxide chemistry. *Science* **371**, 46–51 (2021).
- Zhu, Z. et al. Rechargeable batteries for grid scale energy storage. *Chem. Rev.* **122**, 16610–16751 (2022).
- Liang, Y. L., Dong, H., Aurbach, D. & Yao, Y. Current status and future directions of multivalent metal-ion batteries. *Nat. Energy* **5**, 646–656 (2020).
- Sui, Y. & Ji, X. Anticatalytic strategies to suppress water electrolysis in aqueous batteries. *Chem. Rev.* **121**, 6654–6695 (2021).
- Shinde, S. S. et al. Ampere-hour-scale zinc-air pouch cells. *Nat. Energy* **6**, 592–604 (2021).
- Wang, M. et al. Toward dendrite-free and anti-corrosion Zn anodes by regulating a bismuth-based energizer. *eScience* **2**, 509–517 (2022).
- Cao, L. et al. Highly reversible aqueous zinc batteries enabled by zincophilic-zincophobic interfacial layers and interrupted hydrogen-bond electrolytes. *Angew. Chem., Int. Ed.* **60**, 2–9 (2021).
- Li, C. P., Xie, X. S., Liang, S. Q. & Zhou, J. Issues and future perspective on zinc metal anode for rechargeable aqueous zinc-ion batteries. *Energy Environ. Mater.* **3**, 146–159 (2020).
- Ma, L. et al. Toward practical high-areal-capacity aqueous zinc-metal batteries: quantifying hydrogen evolution and a solid-ion conductor for stable zinc anodes. *Adv. Mater.* **33**, 2007406 (2021).
- Chao, D. & Qiao, S.-Z. Toward high-voltage aqueous batteries: super- or low-concentrated electrolyte? *Joule* **4**, 1846–1851 (2020).
- Kao-ian, W. et al. Stability enhancement of zinc-ion batteries using non-aqueous electrolytes. *Batteries Supercaps* **5**, 202100361 (2022).
- Chan, C. Y. et al. Single-ion conducting double-network hydrogel electrolytes for long cycling zinc-ion batteries. *ACS Appl. Mater. Interfaces* **13**, 30594–30602 (2021).
- Dueramae, I., Okhawilai, M., Kasemsiri, P., Uyama, H. & Kita, R. Properties enhancement of carboxymethyl cellulose with thermoresponsive polymer as solid polymer electrolyte for zinc ion battery. *Sci. Rep.* **10**, 12587 (2020).

15. Abbasi, A. et al. Phosphonated graphene oxide-modified polyacrylamide hydrogel electrolytes for solid-state zinc-ion batteries. *Electrochim. Acta* **435**, 141365 (2022).
16. Zhang, T. S. et al. Fundamentals and perspectives in developing zinc-ion battery electrolytes: a comprehensive review. *Energy Environ. Sci.* **13**, 4625–4665 (2020).
17. Wang, Z. et al. A metal-organic framework host for highly reversible dendrite-free zinc metal anodes. *Joule* **3**, 1289–1300 (2019).
18. Zhao, R. et al. Lanthanum nitrate as aqueous electrolyte additive for favourable zinc metal electrodeposition. *Nat. Commun.* **13**, 3252 (2022).
19. Cao, L. et al. Fluorinated interphase enables reversible aqueous zinc battery chemistries. *Nat. Nanotechnol.* **16**, 902–910 (2021).
20. Han, D. et al. A non-flammable hydrous organic electrolyte for sustainable zinc batteries. *Nat. Sustain.* **5**, 205–213 (2021).
21. Wang, F. et al. Demonstrating U-shaped zinc deposition with 2D metal-organic framework nanoarrays for dendrite-free zinc batteries. *Energy Storage Mater.* **50**, 641–647 (2022).
22. Zhong, C. et al. Decoupling electrolytes towards stable and high-energy rechargeable aqueous zinc–manganese dioxide batteries. *Nat. Energy* **5**, 440–449 (2020).
23. Yang, Z. et al. Electrochemical energy storage for green grid. *Chem. Rev.* **11**, 3577–3613 (2011).
24. Liang, G. et al. Gradient fluorinated alloy to enable highly reversible Zn-metal anode chemistry. *Energy Environ. Sci.* **15**, 1086–1096 (2022).
25. Guo, R. et al. Large-scale integration of zinc metasilicate interface layer guiding well-regulated Zn deposition. *Adv. Mater.* **34**, 2202188 (2022).
26. Yu, Z. et al. Molecular design for electrolyte solvents enabling energy-dense and long-cycling lithium metal batteries. *Nat. Energy* **5**, 526–533 (2020).
27. Niu, C. et al. High-energy lithium metal pouch cells with limited anode swelling and long stable cycles. *Nat. Energy* **4**, 551–559 (2019).
28. Zhou, J. et al. Establishing thermal infusion method for stable zinc metal anodes in aqueous zinc-ion batteries. *Adv. Mater.* **34**, 2200782 (2022).
29. Zhang, Q. et al. Modulating electrolyte structure for ultralow temperature aqueous zinc batteries. *Nat. Commun.* **11**, 4463 (2020).
30. Lu, Y. et al. Ultrasensitive detection of electrolyte leakage from lithium-ion batteries by ionically conductive metal-organic frameworks. *Matter* **3**, 904–919 (2020).
31. Ju, J. et al. Leakage-proof electrolyte chemistry for a high-performance lithium-sulfur battery. *Angew. Chem., Int. Ed.* **60**, 16487–16491 (2021).
32. Qin, Y., Li, H., Han, C., Mo, F. & Wang, X. Chemical welding of electrode-electrolyte interface by Zn metal-initiated in-situ gelation for ultralong-life Zn-ion batteries. *Adv. Mater.* **34**, 2207118 (2022).
33. Liu, Q. et al. Steric molecular combing effect enables ultrafast self-healing electrolyte in quasisolid-state zinc-ion batteries. *ACS Energy Lett.* **7**, 2825–2832 (2022).
34. Liu, Q. et al. Elastomer-alginate interface for high-power and high-energy Zn metal anodes. *Adv. Energy Mater.* **12**, 2200318 (2022).
35. Wang, J. et al. Flexible and anti-freezing zinc-ion batteries using a guar-gum/sodium-alginate/ethylene-glycol hydrogel electrolyte. *Energy Storage Mater.* **41**, 599–605 (2021).
36. Liu, Q. et al. Dual-network structured hydrogel electrolytes engaged solid-state rechargeable Zn-air/iodide hybrid batteries. *Angew. Chem. Int. Ed.* **61**, 202210567 (2022).
37. Zhao, L., Wang, Y., Zhao, X., Deng, Y. & Xia, Y. Facile synthesis of nitrogen-doped carbon quantum dots with chitosan for fluorescent detection of Fe³⁺. *Polymers* **11**, 1731 (2019).
38. Yang, J. L. et al. Stable zinc anode enabled by zincophilic poly-anionic hydrogel layer. *Adv. Mater.* **34**, 2202382 (2022).
39. Shao, Y. et al. Regulating interfacial ion migration via Wool keratin mediated biogel electrolyte toward robust flexible Zn-ion batteries. *Small* **18**, 2107163 (2022).
40. Deng, Y. et al. Fast gelation of Ti₃C₂T_x MXene initiated by metal ions. *Adv. Mater.* **31**, 1902432 (2019).
41. Li, D. et al. Double-helix structure in carrageenan-metal hydrogels: a general approach to porous metal sulfides/carbon aerogels with excellent sodium-ion storage. *Angew. Chem. Int. Ed.* **55**, 15925–15928 (2016).
42. Ji, D. et al. Superstrong, superstiff, and conductive alginate hydrogels. *Nat. Commun.* **13**, 3019 (2022).
43. Evans, J., Vincent, C. A. & Bruce, P. G. Electrochemical measurement of transference numbers in polymer electrolytes. *Polymer* **28**, 2324–2328 (1987).
44. Qiu, H. Y. et al. Zinc anode-compatible in-situ solid electrolyte interphase via cation solvation modulation. *Nat. Commun.* **10**, 5374 (2019).
45. Xie, X. S. et al. Manipulating the ion-transfer kinetics and interface stability for high-performance zinc metal anodes. *Energy Environ. Sci.* **13**, 503–510 (2020).
46. Zhou, L. et al. Suppressing hydrogen evolution in aqueous lithium-ion batteries with double-site hydrogen bonding. *ACS Energy Lett.* **8**, 40–47 (2022).
47. Yang, W., Yang, Y., Yang, H. & Zhou, H. Regulating water activity for rechargeable zinc-ion batteries: progress and perspective. *ACS Energy Lett.* **7**, 2515–2530 (2022).
48. Zhao, Z. et al. Long-life and deeply rechargeable aqueous Zn anodes enabled by multifunctional brightener-inspired interphase. *Energy Environ. Sci.* **12**, 1938–1949 (2019).
49. Liu, Y. et al. Rechargeable aqueous Zn-based energy storage devices. *Joule* **5**, 2845–2903 (2021).
50. Leng, K. et al. A safe polyzwitterionic hydrogel electrolyte for long-life quasi-solid state zinc metal batteries. *Adv. Funct. Mater.* **30**, 2001317 (2020).
51. Hao, Y. et al. Gel electrolyte constructing Zn (002) deposition crystal plane toward highly stable Zn anode. *Adv. Sci.* **9**, 2104832 (2022).
52. Wei, T. et al. Bonding interaction regulation in hydrogel electrolyte enable dendrite-free aqueous zinc-ion batteries from –20 to 60 °C. *Chem. Eng. J.* **434**, 134646 (2022).
53. Zeng, X. et al. Bio-inspired design of an in situ multifunctional polymeric solid-electrolyte interphase for Zn metal anode cycling at 30 mA cm⁻² and 30 mA h cm⁻². *Energy Environ. Sci.* **14**, 5947–5957 (2021).
54. Cong, J. L. et al. Ultra-stable and highly reversible aqueous zinc metal anodes with high preferred orientation deposition achieved by a polyanionic hydrogel electrolyte. *Energy Storage Mater.* **35**, 586–594 (2021).
55. Chen, M. et al. Realizing an all-round hydrogel electrolyte toward environmentally adaptive dendrite-free aqueous Zn-MnO₂ batteries. *Adv. Mater.* **33**, 2007559 (2021).
56. Huang, S., Hou, L., Li, T., Jiao, Y. & Wu, P. Antifreezing hydrogel electrolyte with ternary hydrogen bonding for high-performance zinc-ion batteries. *Adv. Mater.* **34**, 2110140 (2022).
57. Zhou, J. et al. Encapsulation of metallic Zn in hybrid MXene/graphene aerogel as stable Zn anode for foldable Zn-ion batteries. *Adv. Mater. Inter.* **34**, 2106897 (2021).
58. Qin, R. et al. Tuning Zn²⁺ coordination environment to suppress dendrite formation for high-performance Zn-ion batteries. *Nano Energy* **80**, 105478 (2021).
59. Kundu, D., Adams, B. D., Duffort, V., Vajargah, S. H. & Nazar, L. F. A high-capacity and long-life aqueous rechargeable zinc battery using a metal oxide intercalation cathode. *Nat. Energy* **1**, 16119 (2016).

60. Zhang, Y. et al. Separator effect on zinc electrodeposition behavior and its implication for zinc battery lifetime. *Nano Lett.* **21**, 10446–10452 (2021).
61. Yang, X., Deng, W., Chen, M., Wang, Y. & Sun, C. F. Mass-producible, quasi-zero-strain, lattice-water-rich inorganic open-frameworks for ultrafast-charging and long-cycling zinc-ion batteries. *Adv. Mater.* **32**, 2003592 (2020).
62. Chen, Y. et al. Low current-density stable zinc-metal batteries via aqueous/organic hybrid electrolyte. *Batteries Supercaps* **5**, 202200001 (2022).
63. Chen, Z. et al. Polymeric single ion conductors with enhanced side chains motion for high-performance solid zinc ion batteries. *Adv. Mater.* **34**, 2207682 (2022).
64. Ma, G. et al. Reshaping the electrolyte structure and interface chemistry for stable aqueous zinc batteries. *Energy Storage Mater.* **47**, 203–210 (2022).
65. Zhang, H. et al. Inducing the preferential growth of Zn (002) plane for long cycle aqueous Zn-Ion batteries. *Adv. Energy Mater.* **13**, 2203254 (2022).
66. Li, M. et al. Comprehensive H₂O molecules regulation via deep eutectic solvents for ultra-stable zinc metal anode. *Angew. Chem. Int. Ed.* **62**, 202215552 (2023).
67. Lin, Y. et al. Dendrite-free Zn anode enabled by anionic surfactant-induced horizontal growth for highly-stable aqueous Zn-ion pouch cells. *Energy Environ. Sci.* **16**, 687–697 (2023).
68. Lu, H., Zhou, J., Ye, G. & Zhou, X. Recent advances in continuous models of electrochemical supercapacitors. *J. Electrochem.* **24**, 517–528 (2018).
69. Su, Y. et al. Rational design of a topological polymeric solid electrolyte for high-performance all-solid-state alkali metal batteries. *Nat. Commun.* **13**, 4181 (2022).
- characterizations and electrochemical measurements. H.Z., Z.C., L.W., W.L., J.S., and J.Y., contributed to the structural characterizations and electrochemical measurements. H.L. carried out the finite simulation. F.W., C.Y. Z.W., and Q.-H.Y. organized and wrote the manuscript. All authors contributed to the discussion and revision of the manuscript.

Competing interests

The authors declare no competing interests.

Additional information

Supplementary information The online version contains supplementary material available at <https://doi.org/10.1038/s41467-023-39877-5>.

Correspondence and requests for materials should be addressed to Chunpeng Yang or Quan-Hong Yang.

Peer review information *Nature Communications* thanks the anonymous reviewers for their contribution to the peer review of this work. A peer review file is available.

Reprints and permissions information is available at <http://www.nature.com/reprints>

Publisher's note Springer Nature remains neutral with regard to jurisdictional claims in published maps and institutional affiliations.

Open Access This article is licensed under a Creative Commons Attribution 4.0 International License, which permits use, sharing, adaptation, distribution and reproduction in any medium or format, as long as you give appropriate credit to the original author(s) and the source, provide a link to the Creative Commons licence, and indicate if changes were made. The images or other third party material in this article are included in the article's Creative Commons licence, unless indicated otherwise in a credit line to the material. If material is not included in the article's Creative Commons licence and your intended use is not permitted by statutory regulation or exceeds the permitted use, you will need to obtain permission directly from the copyright holder. To view a copy of this licence, visit <http://creativecommons.org/licenses/by/4.0/>.

© The Author(s) 2023

Acknowledgements

This research was supported by grants from the National Key Research and Development Program of China (No. 2022YFB2404500). We also appreciate the funding supports from the Haihe Laboratory of Sustainable Chemical Transformations, National Industry-Education Integration Platform of Energy Storage, and the Fundamental Research Funds for the Central Universities.

Author contributions

Q.-H.Y. and C.Y. supervised the project. C.Y. and F.W. conceived the idea. F.W. and J.Z. synthesized the materials and performed the